Numerical simulation of the transient aerodynamic phenomena induced by passing manoeuvres

David Uystepruyst, Siniša Krajnović

Numerical simulation of the transient aerodynamic phenomena induced by passing manoeuvres

David Uystepruyst[a], Siniša Krajnović[a]

[a]*Division of Fluid Dynamics, Department of Applied Mechanics, Chalmers University of Technology, SE-41296 Gothenburg, Sweden.*

Abstract

Several three-dimensional Unsteady Reynolds-Averaged Navier-Stokes (URANS) simulations of the passing generic vehicles (Ahmed bodies) are presented. The relative motion of vehicles was obtained using a combination of deforming and sliding computational grids. Two different vehicle bodies were studied having an angle of the rear end slanted surface of 30° and 0°. Several different relative velocities and transversal distances between vehicles were studied. Aerodynamic influence of the passage on both the overtaken and the overtaking vehicles was studied. The results of the simulations were found to agree well with the existing experimental data.

Keywords: Passing manœuvres, Overtaking vehicles, Unsteady aerodynamics, Navier-Stokes equations, turbulence model, Deforming mesh, Sliding mesh

1. Introduction

Two vehicles moving in close proximity mutually influence their aerodynamic fields. This influence occurs like additional forces acting on both vehicles, especially side forces and yawing moments. Forces intensities de-

pend essentially on the relative velocity, the transversal spacing and the size ratio between both vehicles. The prompt evolutions around the yaw axis constrain trajectory corrections to be performed by the driver and can yield critical safety situations, in particular in adverse weather conditions, such as crosswinds.

Since 1970's, overtaking and crossing effects of two vehicles have been investigated experimentally. Early studies coincide with the first oil crisis, i.e. 1973 for Heffrey [1] and Howell [2]. Indeed, this crisis involved a need to reduce the oil consumption, especially by the reduction of vehicle weight. Being lighter, vehicles became more sensitive to the unsteady aerodynamic effects.

In addition to works of Heffrey and Howell, several experimental studies have been carried out. These studies are interested by different aspects. Studies of Legouis *et al* [3], Telionis *et al* [4] or Yamamoto *et al* [5] are particularly dedicated to the car-truck overtaking process showing the importance of the size ratio.

More recently, Noger and his collaborators performed several dynamic studies in order to analyze effects of the relative velocity, the transverse passing and the crosswind when two vehicles overtake: Noger and Széchényi [6] and Noger *et al* [7]. Both studies were carried out with a 7/10 scaled Ahmed bodies, see Ahmed *et al* [8]. The bodies of the first study are hatchback shapes (slant of 30°), while the bodies of the second one are squareback shapes. Noger and Van Grevenynghe [9] proposed a study of car-truck overtaking on one test case. Gilliéron and Noger [10] analyzed the transient phenomena occurring during various phenomena such as the overtaking, the crossing or the tunnel

exit.

Some recent two-dimensional (2D) numerical studies can be found. Clark and Filippone [11] performed the overtaking process of two sharp edges bodies. The work aimed to give thorough analysis of the overtaking process. Effects of the relative velocity and the transversal spacing were studied. Authors focused on 2D overtaking as a preliminary means of investigating an appropriate simulation strategy for the complex three-dimensional (3D) flow. Corin *et al* [12] used rounded edges bodies. The dynamic effect of the passing manoeuvre was highlighted by comparisons with quasi-steady calculations. It was shown that crosswinds yield significant dynamic effects. The authors of [11, 12] agreed that their 2D approaches were first step towards 3D calculations. In particular, the Venturi effect, occurring when vehicles getting closer, was strongly overestimated.

Gilliéron [13] performed a 3D numerical simulation of two Ahmed bodies overtaking. Calculations were achieved using a Reynolds Averaged Navier-Stokes numerical method with a $k - \epsilon$ turbulence model. The effects of the transversal spacing and the crosswind were studied. However, this study was limited to a steady approach.

In summary, no dynamic 3D numerical method is available yet. The development of a 3D methodology seems, therefore, important to improve the knowledges and to plan further studies. This paper presents a three-dimensional simulation of passing processes based on the $\zeta - f$ turbulence model and a deforming/sliding mesh method. The main work aims to accurately predict the aerodynamic forces and moment and to give a thorough analysis of the passing process. The paper starts with a description in chapter 2 of the

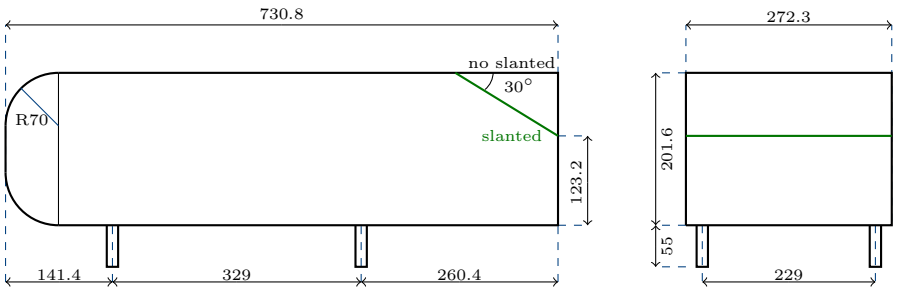

Figure 1: 7/10 scale Ahmed bluff body, dimensions in mm.

experimental set-up that is used in the present numerical study. In chapter 3, the dimensionless coefficients, allowing to quantify the phenomena and to make the validation, are then presented. This is followed by the numerical methodology, including the turbulence model, the numerical method and details, and the deforming/sliding mesh method, in chapter 4. Results of the simulations are presented in chapter 5.

2. The set-up

2.1. Geometries

The body used in this study is identical to this in the experimental work [7] and is 7/10 Ahmed bodies shown in figure 1. This body has a hatchback type rear end with an angle of 30°. The last chapter of the paper presents the overtaking of two squareback shape bodies, same as in [6], i.e. with no slanted surface.

As it is shown, both bodies consist on rounded front end and sharped rear end. The main vehicle sizes are: the length $L = 730.8\ mm$, the width $W = 272.3\ mm$, the height $H = 201.6\ mm$ and the ground clearance of $55\ mm$. Supports are $15\ mm$ diameter cylindrical and the length of the slant

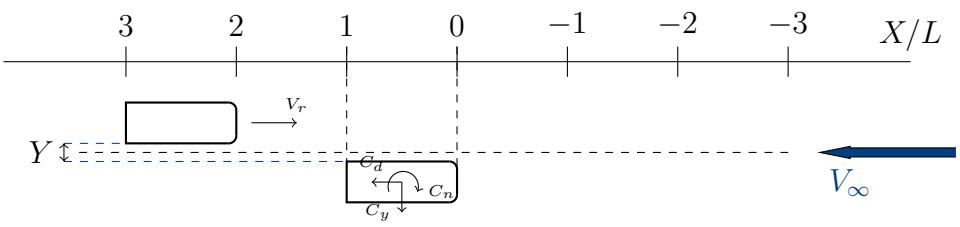

Figure 2: Notations for the vehicle positioning and aerodynamic coefficient direction.

surface is 155.4 mm. The Reynolds number based on height of the vehicle is $Re_H = 390.000$, for a velocity of 30 $m.s^{-1}$.

2.2. Overtaking process

The figure 2 shows the sketch of the overtaking, with distances and the forces direction. The overtaking consist, as in the experimental work, on the stationnary body located in the middle of the wind tunnel length and a moving body located 5L backward the stationnary one at the beginning, and 5L forward at the end of the calculation. An inlet condition is set with the normal velocity V_∞ corresponding to the velocity of the stationnary body. The moving body is set in motion with the relative velocity V_r. Except for the following chapters on the relative velocity effect, on the transverse spacing effect and on the overtaking vehicle; the velocity ratio k and the transversal spacing Y are fixed at the values $k = 0.248$ ($V_\infty = 30.32$ $m.s^{-1}$ and $V_r = 10$ $m.s^{-1}$) and $Y = 0.25W$.

3. Dimensionless coefficient

As in the experimental works of Noger *et al*, a dimensionless parameter k is defined as the ratio of the relative velocity V_r to a steady velocity V:

$$k = \frac{V_r}{V}. \tag{1}$$

The steady velocity is the velocity of the moving body, *e.g.* for the overtaking simulations, the steady velocity is $V = V_\infty + V_r$.
During an overtaking, the strongly affected aerodynamic coefficients are the drag force coefficient C_d, the side force coefficient C_y and the yawing moment coefficient C_n given by:

$$\begin{cases} F_d = \frac{1}{2}\rho S V^2 C_d, \\ F_y = \frac{1}{2}\rho S V^2 C_y, \\ N = \frac{1}{2}\rho E S V^2 C_n, \end{cases} \tag{2}$$

where F_d, F_y and N are respectively the drag force, the side force and the yawing moment obtained by integrating the pressure distribution around the model. In equation (2), ρ is the air density, S the body frontal area and E the wheelbase. Note that V is the previous steady velocity.

4. Numerical methodology

4.1. Governing equations and turbulence model

The flow around vehicles is unsteady, three-dimensional, incompressible (the Mach number is $M \simeq 0.1$), viscous and turbulent. In order to simulate it, the three-dimensional equations of Navier-Stokes have to be resolved with

turbulence modeling. The Reynolds Averaged Navier Stokes equations are given as follows:

$$\begin{cases} \dfrac{\partial U_i}{\partial x_i} = 0, \\ \dfrac{\partial U_i}{\partial t} + U_j \dfrac{\partial U_i}{\partial x_j} = -\dfrac{1}{\rho}\dfrac{\partial P}{\partial x_i} + \dfrac{1}{\rho}\dfrac{\partial}{\partial x_j}\left(\tau_{ij} - \rho\overline{u_i u_j}\right), \end{cases} \tag{3}$$

where U_i is the mean-velocity vector, ρ is the fluid density, P the mean-pressure, τ_{ij} denotes the mean viscous stress tensor:

$$\tau_{ij} = 2\mu S_{ij}. \tag{4}$$

In the equation (4), μ is the dynamic viscosity and the mean strain rate tensor S_{ij} is given by:

$$S_{ij} = \frac{1}{2}\left(\frac{\partial U_i}{\partial x_j} + \frac{\partial U_j}{\partial x_i}\right).$$

The last term of equation (3) is the unknown Reynolds stress tensor resulting on the fluctuating part of the Reynolds average which must be modeled. The vehicle overtaking process is a transient physical phenomenon, with a physical time of several seconds and a body displacement, which requires an important computational effort. Accurate numerical methods, as LES for example, remain too ambitious for the nowadays computer capability and turbulence modelling is preferred [11, 12, 13]. The $\zeta - f$ model developed by Hanjalić *et al* [14] seems to be a good compromise between two equations models and second order models. This model is based on the $\overline{v^2} - f$ model of Durbin [15] which is able to predict the near-wall turbulence anisotropy by expressing the turbulent viscosity as a function of the turbulent kinetic energy k and its dissipation ε, and a turbulent velocity scale $\overline{v^2}$ instead of k.

However, the $\overline{v^2}-f$ model is numerically unstable for too small y^+. To resolve this problem, Hanjalić *et al* [14] proposed to solve a transport equation for the velocity scale ratio $\zeta = \overline{v^2}/k$ instead of $\overline{v^2}$.

First, the Reynolds stress tensor is expressed with the Boussinesq's analogy:

$$-\rho\overline{u_i u_j} = 2\rho\nu_t S_{ij} - \frac{2}{3}\rho k\delta_{ij},$$

where ν_t is the turbulent viscosity, δ_{ij} is the Kronecker delta. In the $\zeta - f$ model, the eddy-viscosity is defined as:

$$\nu_t = C_\mu \zeta k \tau,$$

where τ is the time scale given as:

$$\tau = \max\left[\min\left(\frac{k}{\varepsilon}, \frac{a}{\sqrt{6}C_\mu\left|S\right|\zeta}\right), C_\tau\left(\frac{\nu}{\varepsilon}\right)^{1/2}\right].$$

The velocity scale ratio ζ is obtained from the following equation:

$$\frac{D\zeta}{Dt} = f - \frac{\zeta}{k}\mathcal{P}_k + \frac{\partial}{\partial x_k}\left[\left(\nu + \frac{\nu_t}{\sigma_\zeta}\right)\frac{\partial\zeta}{\partial x_k}\right].$$

The equations of the turbulent kinetic energy and its dissipation are:

$$\frac{Dk}{Dt} = (\mathcal{P}_k - \varepsilon) + \frac{\partial}{\partial x_j}\left[\left(\nu + \frac{\nu_t}{\sigma_k}\right)\frac{\partial k}{\partial x_j}\right]$$

$$\frac{D\varepsilon}{Dt} = \frac{C_{\varepsilon 1}\mathcal{P}_k - C_{\varepsilon 2}\varepsilon}{\tau} + \frac{\partial}{\partial x_j}\left[\left(\nu + \frac{\nu_t}{\sigma_\varepsilon}\right)\frac{\partial\varepsilon}{\partial x_j}\right].$$

In above equations, the production is given by:

$$\mathcal{P}_k = -\overline{u_i u_j}\frac{\partial U_i}{\partial x_j}.$$

The elliptic relaxation function f is formulated by using the pressure-strain mode of Speziale *et al* [16]:

$$L^2\nabla^2 f - f = \frac{1}{\tau}\left(c_1 + C_2'\frac{\mathcal{P}_k}{\epsilon}\right)\left(\zeta - \frac{2}{3}\right) - \left(\frac{C_4}{3} - C_5\right)\frac{\mathcal{P}_k}{k}.$$

C_μ	$C_{\varepsilon 1}$	$C_{\varepsilon 2}$	c_1	C_2'	σ_k	σ_ε	σ_ζ	C_τ	C_L	C_η
0.22	$1.4(1+0.012/\zeta)$	1.9	0.4	0.65	1	1.3	1.2	6.0	0.36	85

Table 1: Coefficients in the $\zeta - f$ turbulence model

The length scale L is:

$$L = C_L \max\left[\min\left(\frac{k^{3/2}}{\varepsilon}, \frac{k^{1/2}}{\sqrt{6}C_\mu\left|S\right|\zeta}\right), C_\eta\left(\frac{\nu^3}{\varepsilon}\right)^{1/4}\right].$$

Coefficients in above equations are given in table 1.

4.2. Numerical method and boundary conditions

The couple of equations (3) was solved using a commercial solver, AVL FIRE. This software is based on a cell-centered finite volume method. The momentum equations were discretized using a second-order upwind scheme. An implicit second-order scheme was used for the temporal discretization. The SIMPLE algorithm was used to couple the velocity and pressure fields. A collocated grid arrangement was employed.

The numerical domain is shown in figure 3. The experimental wind tunnel section is 5 m × 3 m and is cut in the numerical simulation. The width, and the height, of the numerical domain represent respectively more than 11 times, and 5.5 times, the width of the vehicle. The length is set to 18 m for the good progress of the deforming/sliding mesh strategy.

The uniform free stream velocity V_∞ was set at the inlet boundary, in front of vehicles. A static pressure was applied at the outlet. No-slip wall boundary conditions were used on the bodies and on the floor. Finally, slip wall boundary conditions were applied on the lateral and on the roof surfaces.

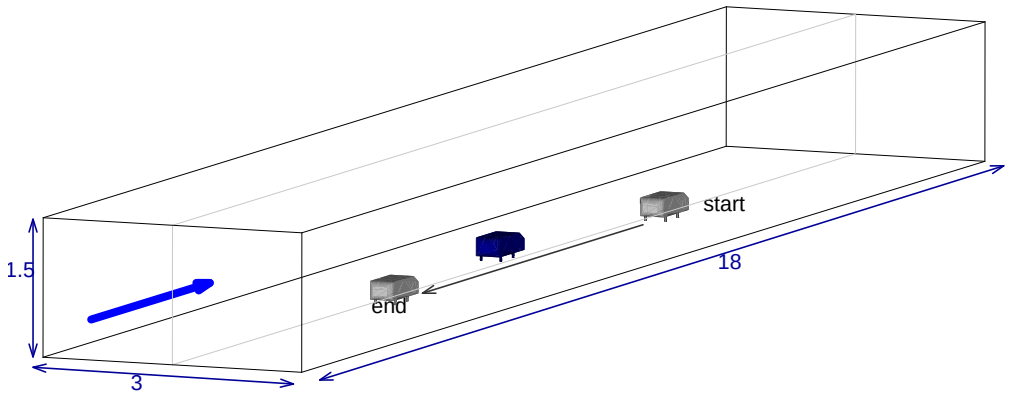

Figure 3: Computational domain (dimensions in m).

4.3. Numerical details

The structured grids were made with the commercial grid generator Ansys ICEM-CFD and consist of only hexahedral elements. The figure 4 shows a side view of volume and surface meshes, for both bluff bodies. A grid topology was constructed using several O-grids in order to concentrate most of the computational cells close to the surface of the vehicles.

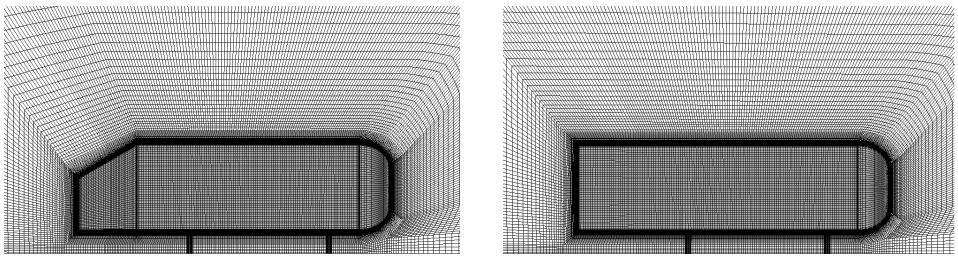

(a) slanted Ahmed body (b) 0° rear end Ahmed body

Figure 4: Surface and volume mesh of bluff bodies.

For the same resolution, the number of elements of the slanted body mesh is

coarse	middle	fine
$20 < \Delta s^+ < 960$	$20 < \Delta s^+ < 580$	$20 < \Delta s^+ < 500$
$20 < \Delta l^+ < 840$	$20 < \Delta l^+ < 560$	$20 < \Delta l^+ < 450$

Table 2: Resolution in the streamwise and normal streamwise directions.

slightly more important due to a fine mesh necessity at the slant region. Accuracy was established by making the original case simulation ($k = 0.248$ and $Y = 0.25W$) on three different computational grids. The numbers of elements are: 4 millions for the coarse mesh, 6 millions for the middle mesh and 8 millions for the fine mesh. For a velocity of 30 $m.s^{-1}$, the wall normal resolution, n^+, is such that $n^+ < 2$, $n^+ < 4$ and $n^+ < 6$ for the fine mesh, the middle mesh and the coarse mesh respectively. Note that the cell next to the wall should reach n^+ as a maximum less than 3 with the $\zeta - f$ model. The resolution in the streamwise direction Δs^+, and the resolution in directions normal to streamwise Δl^+ are reported in table 2 for the three computational meshes. The time step was 5×10^{-4} s giving a CFL number around 0.9 for the highest velocity.

4.4. Deforming and sliding mesh

The rectilinear displacement of a body is generally achieved by a sliding mesh method. Indeed, this method is less time consumming than other methods like overlapping meshes method for example. However, a sliding method demands a specific treatment of the boundaries, like moving downstream and upstream boundaries or periodic boundary conditions. The technique consisting on the combination of a sliding and a deforming methods, and already used by Krajnović *et al* [17], allows to obtain the efficiency of the sliding

method while it is keeping the initial domain and the initial boundaries. The resulting computational grids are illustrated in figure 5 for three different times of the simulation.

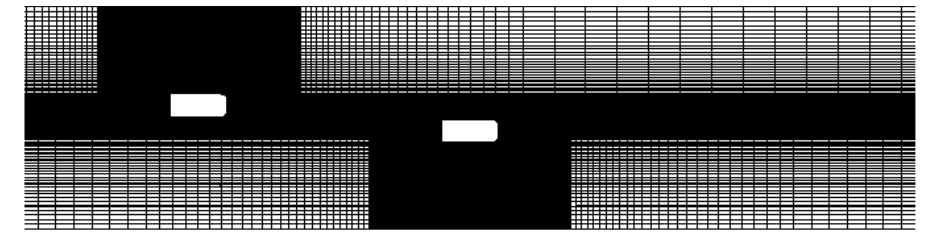

(a) start

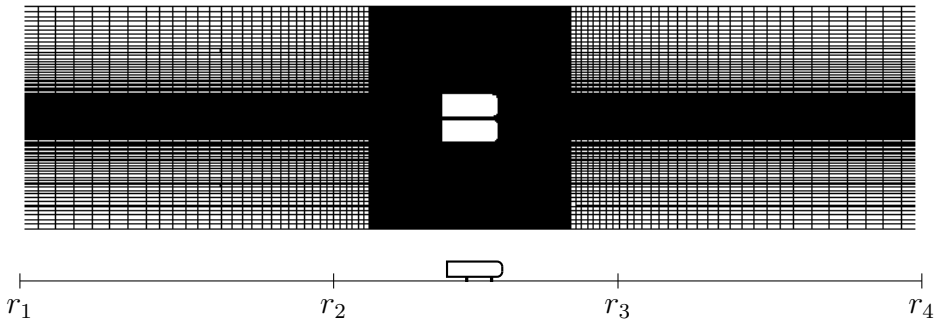

(b) middle

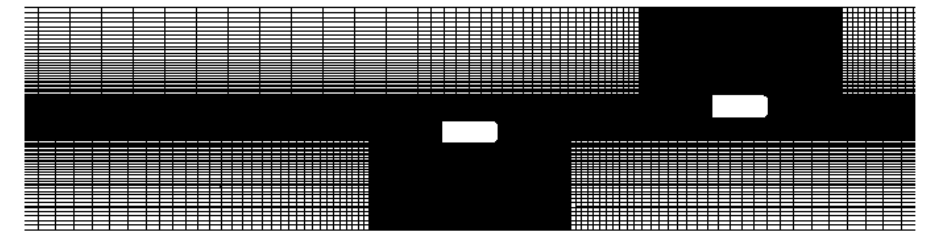

(c) end

Figure 5: Deformation of the computational grid for the overtaking process.

The overall domain is composed by two subdomains: the bottom one, containing the stationnary body, remains fixed all along the simulation; and the

top one, containing the moving body, is created by a mirror of the bottom mesh and is subdivided in three zones, see the figure 5(b).

The part of the mesh between r_2 and r_3 is slided during the simulation. The two remaining parts, between r_1 and r_2 and between r_3 and r_4, are deformed. These deformations are compressions or stretching depending on the direction of the translation of the middle part. The slided displacement of the middle part avoids any problems of critical cell sizes and avoids any numerical disturbances resulting from the mesh deformation.

These transformations are applied on the nodes. Let denotes by x the abscissa of any node of the sliding mesh, at the time t the position of x is:

$$\begin{cases} x = x + \delta \dfrac{x - r_1}{r_2 - r_1}, & \text{if } x \in [r_1, r_2[\,, \\ x = x + \delta, & \text{if } x \in [r_2, r_3]\,, \\ x = x + \delta \dfrac{r_4 - x}{r_4 - r_3}, & \text{if } x \in]r_3, r_4]\,, \end{cases}$$

where $\delta = \Delta + V_r t$, and Δ is the initial displacement to place the overtaking vehicle 5L backward. Afterwards, the volume of cells, the area of faces and the centers are updated. Finally a common interfacing is performed between the two meshes.

5. Results

5.1. Mesh resolution

The side force and the yawing moment coefficients obtained on the three meshes, discussed in the section 4.3, are shown in figure 6 and compared to the experimental data.

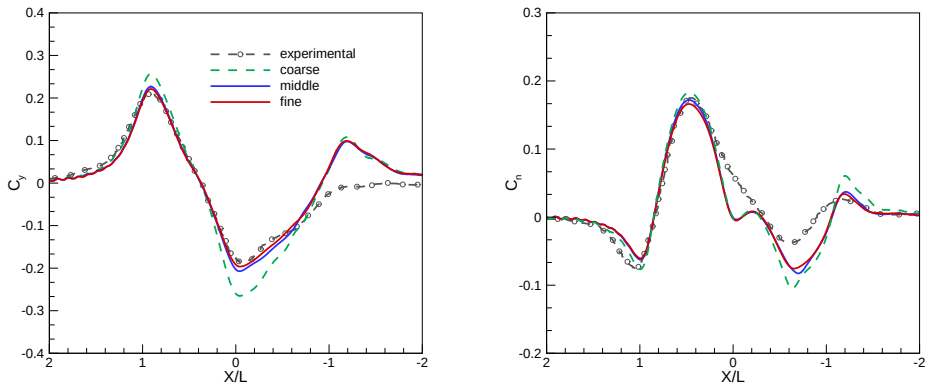

Figure 6: Mesh resolution analysis. Side force (left) and yawing moment (right) coefficients.

As it can be seen, the coarse mesh involves a systematical overestimation of amplitudes, especially on the side force, while the middle and the fine mesh yield quasi similar results: relatively close to the experimental data. For this reason, the middle mesh resolution is considered to be sufficient, as the fine mesh does not bring significant improvements. It can be noted that there are some differences between experimental data and numerical results. These differences are discussed in the next section.

5.2. Coefficients behavior explanation

The figure 7 shows the numerical results obtained for the drag force, the side force and the yawing moment coefficients. On these three graphs, the 5 vertical dashed lines, labelled by ⓑ, ⓒ, ⓓ, ⓔ and ⓕ, correspond to the critical moments for which the changes are substantial and which require explanations.

The evolution of the pressure on the inner side of the overtaken vehicle can bring a first explanation. The pressure distributions are shown in figure 8

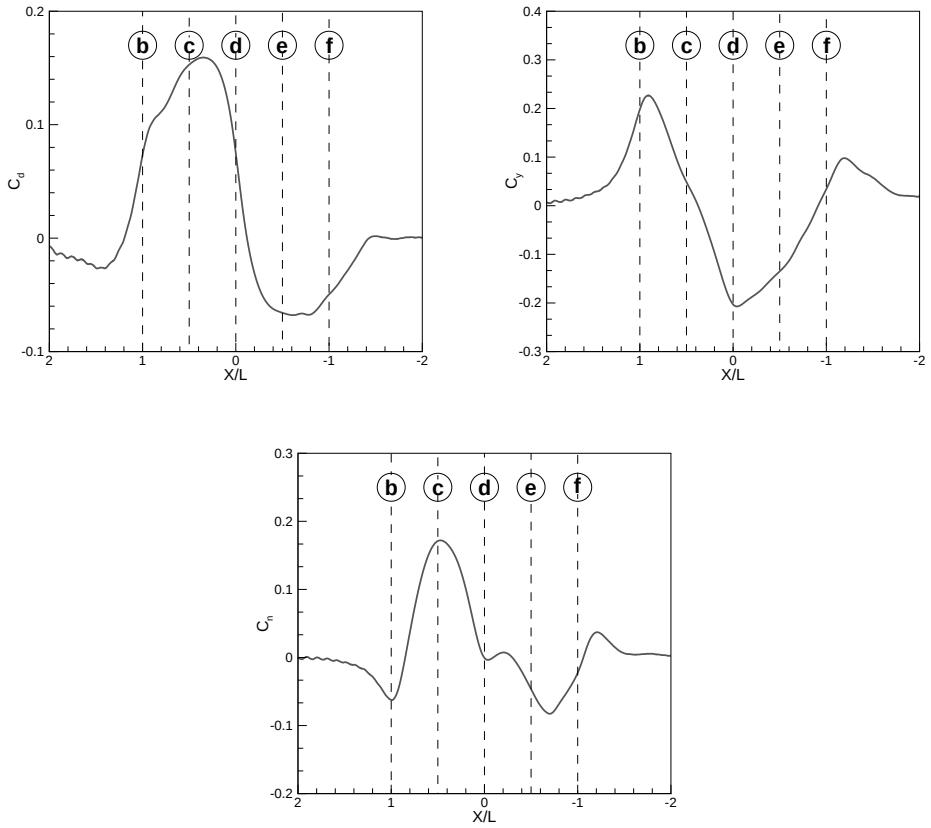

Figure 7: Curves behaviors explanation. Drag force (top left), side force (top right) and yawing moment (bottom) coefficients.

for the five moments corresponding to the vertical lines of figure 7 and for the position $X = 2L$ which shows the steady state pressure, i.e. without the influence of the overtaking vehicle. Similarly, figure 9 presents the instantaneous streamlines of the velocity field projected onto the plane $z = 0.1558\,m$, the half of the total height of the vehicle, for the six previous positions.

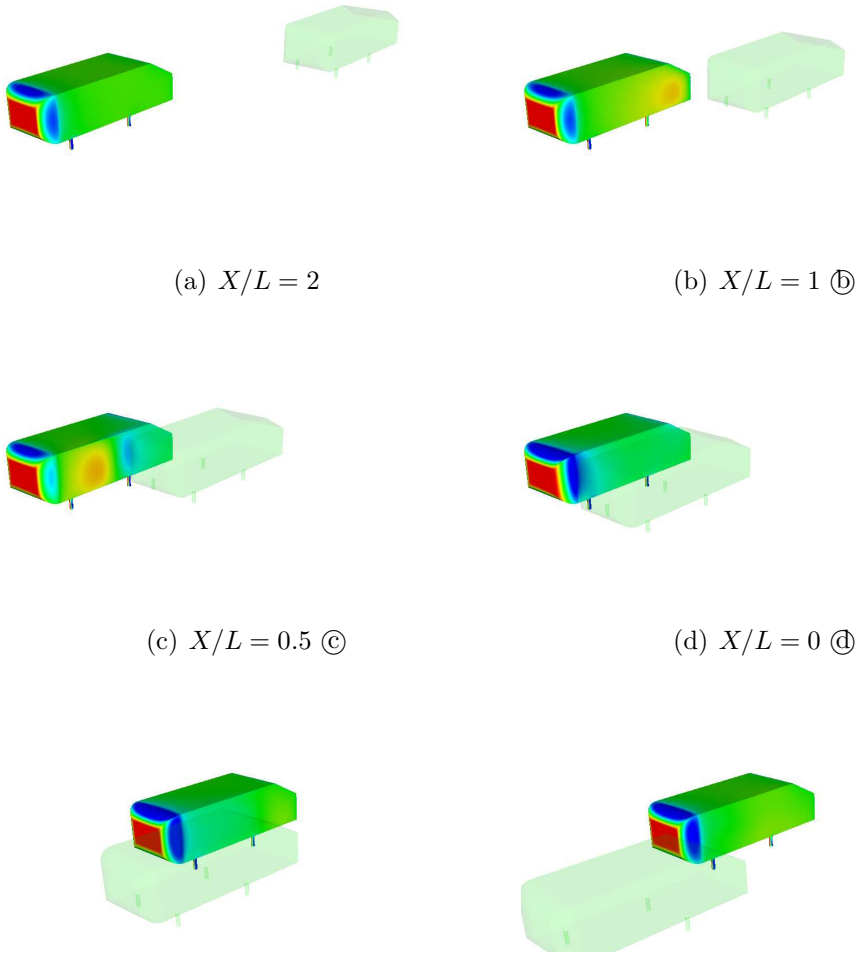

(a) $X/L = 2$ (b) $X/L = 1$ ⓑ

(c) $X/L = 0.5$ ⓒ (d) $X/L = 0$ ⓓ

(e) $X/L = -0.5$ ⓔ (f) $X/L = -1$ ⓕ

Figure 8: Pressure distribution on the overtaken vehicle

5.2.1. Before ⓑ

As it can be seen in figure 9(a), the overtaking body has already an effect on the flow at the aft of the overtaken one at the position X/L=2. This can be identified on the drag coefficient which is decreasing. The positive pressure field in front of the overtaking body involves an increase of the

pressure at the aft of the overtaken body, then a drag reduction. Afterwards, this positive pressure field occurs on the inner side of the overtaken body and repels it, figure 8(b). This effect is, in a first time, concentrated on the rear of the overtaken body. It involves an increase of the side force and a decrease of the yawing moment (anticlockwise moment). Indeed, this positive pressure field is only acting on the rear of the overtaken body, then the rear of overtaken body is repelling. Besides, the overtaking body approach has an effect at the aft of the overtaken body. As it can be seen in figure 9(b), the flow separation from the overtaken body's leading edge is disrupted and the recirculating flow to the aft outer surface is shifted. Theses influences yield a further anticlockwise moment.

In ⓑ, the negative pressure in the front side of the overtaking body reduces the pressure at the aft of the overtaken body. The pressure is reducing all the more than the narrowing of the space between both bodies involves an acceleration of the flow, then a pressure decrease. This low-pressure at the aft of the overtaken body explains the drag pulse recorded.

5.2.2. Between ⓑ and ⓒ

The front of the overtaking body is next to the rear of the overtaken one, then a Venturi effect appears. This Venturi effect is added to the negative pressure on the front side of the overtaking vehicle to make a global low-pressure effect. This yields a decrease of the side force with the reduction of the pressure involved by the Venturi effect, both vehicles are attracted, and an increase of the yawing moment. Indeed, this low-pressure effect is on the rear of the overtaken body, then the rear of this body is pulling into the path of the overtaking body. As the side force is decreasing, it should be noted

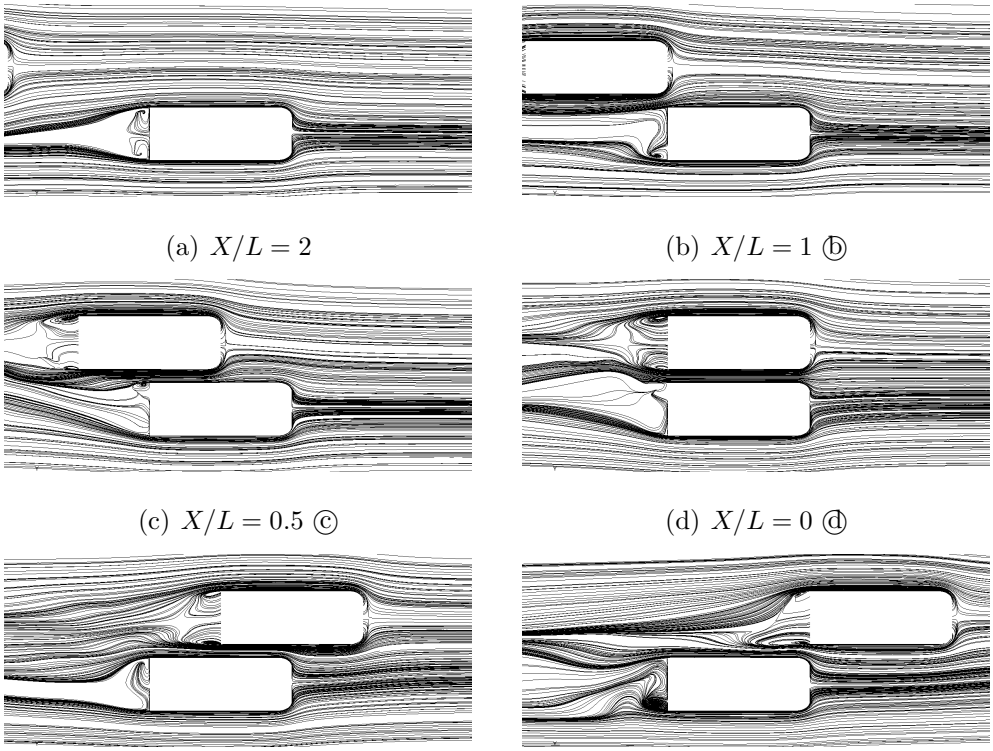

(a) $X/L = 2$ (b) $X/L = 1$ ⓑ

(c) $X/L = 0.5$ ⓒ (d) $X/L = 0$ ⓓ

(e) $X/L = -0.5$ ⓔ (f) $X/L = -1$ ⓕ

Figure 9: Streamlines of the velocity field projected on the plane $z = 0.1558\ m$.

that the maximum is obtained at the position X/L=1.

The positive pressure in front of the overtaking body repels the front part of overtaken one, figure 8(c), which increases further the yawing moment. The combined effects of the low-pressure on the rear half of the overtaken body, and the positive pressure on the front half of the overtaken body lead to the maximum value for the yawing moment in ⓒ, figure 8(c).

5.2.3. Between ⓒ and ⓓ

The overtaking body passed the central region of the overtaken one, the low-pressure effect is now predominating: the side force decreases further and

is now negative; the yawing moment also decreases. Indeed, the low-pressure effect is also acting on the front half of the overtaken body, which means that the nose of the overtaken body is pulling into the path the overtaking one. In ⓓ, figure 8(d), both vehicles are side by side, the low-pressure effect is maximum, which means the side force reaches its minimum value.

5.2.4. Between ⓓ and ⓔ

The low-pressure effect decreases, both vehicles repel each other, then the side force increases. This low-pressure effect is concentrated on the front of the overtaken body. Hence the yawing moment is still decreasing and is now negative. Note that the yawing moment slightly increase just after ⓓ. There is an interaction between the flow separations occurring at the aft edges of both bodies, figure 9(d). The drag coefficient reaches its minimum value due to the low-pressure which is acting on the fore of the overtaken body.

5.2.5. Between ⓔ and ⓕ

The low-pressure effect still decreases: the side force increases and the yawing moment increases.

5.2.6. After ⓕ

When the overtaking body rear passes the front of the overtaken one, both vehicles repel each other: the three coefficients increase. As seen, in figure 10, a positive pressure part, is coming from the rear of the overtaken body towards the overtaken one. The inner sharp edge at the aft of the overtaking body is producing a flow separation which repels the overtaken body. Furthermore, the flow at the aft of the overtaken body, figure 9(f), is similar to the flow at the position X/L=1. The inner flow separation is disrupted by

the flow at the aft of the overtaking body and the outer recirculating flow is shifted. This yield to increase further the yawing moment.

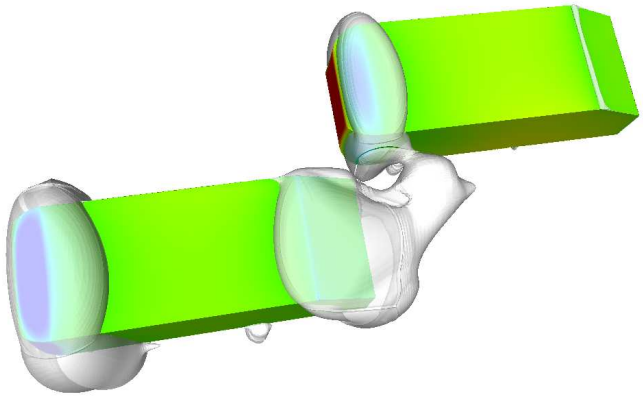

Figure 10: Isosurface of pressure, p=20 Pa. At the position X/L=-1.

Finally, at the position X/L=-2, forces and moment are returned to the equilibrium state.

5.3. Comparison of the numerical results with the experimental data

The first difference, and certainly the most substantial, is the numerical peak of side force around X/L=-1, figure 6, which does not exist in the experimental data. First, it can be noted that this peak appears on experimental results for lower k which are, unfortunately, difficult to consider numerically. This result is inconsistent with the numerical results of Corin *et al* [12] for which rounded edges models are used. However, it is consistent with the numerical results of Clarke and Filippone [11] for which sharp edges are used. Moreover, Gilliéron [13] obtained the same kind of behavior with his simulations of 3D slanted Ahmed bodies. This peak are induced by the

flow separation occurring at the inner sharp edge at the aft of the overtaking body. It should be noted that a RANS turbulence model is not able to reproduce perfectly the flow around a body, especially behind sharp edges. Hence, the effects occurred by sharp edges can be exacerbated.

The second effect is the weak increase of yawing moment at X/L=0: when vehicles are side by side. Actually, such a behavior of the moment curves start to show up for $k = 0.248$, on the experimental data, and it is more substantial for $k = 0.141$ (see figure 11(b)).

Finally, it can be noted that the numerical simulation underestimates the value of the first negative peak of yawing moment and overestimates the second one, see figure 6.

5.4. Relative velocity effects

In the experimental work, 4 relative velocities were studied. Unfortunately, two of them, $k = 0.007$ and $k = 0.076$, involve a low relative velocity, then an important physical time. Hence, it is not possible to make reasonable computational time calculation.

For the comparison, the case with a velocity ratio of $k = 0.141$ ($V_r = 5\ m.s^{-1}$) is performed in addition of the original case $k = 0.248$. The numerical results obtained for these two relative velocities are shown in figure 11 as well as the experimental data.

For both cases, the numerical results are in good agreement with the experimental data. Nevertheless, the overestimation of the first peak of side force by the numerical simulation is slightly more substantial for $k = 0.141$ than for $k = 0.248$. For $k = 0.141$, the numerical result of side force is constant between X/L=0 and X/L=-0.5. However, it is consistent with the experi-

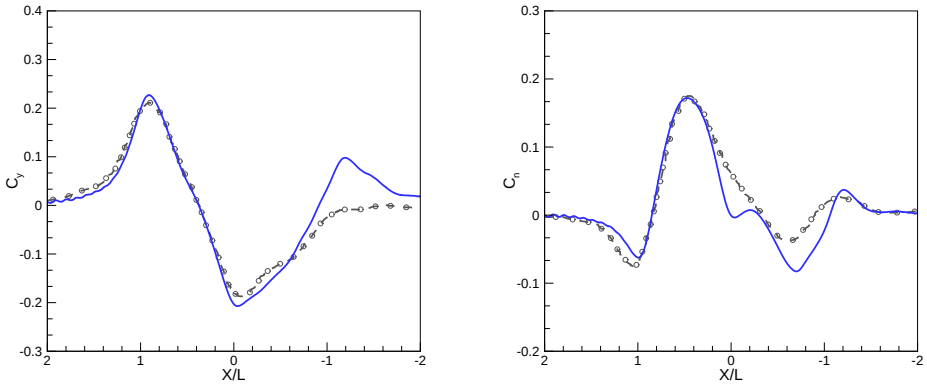

(a) $k = 0.248$

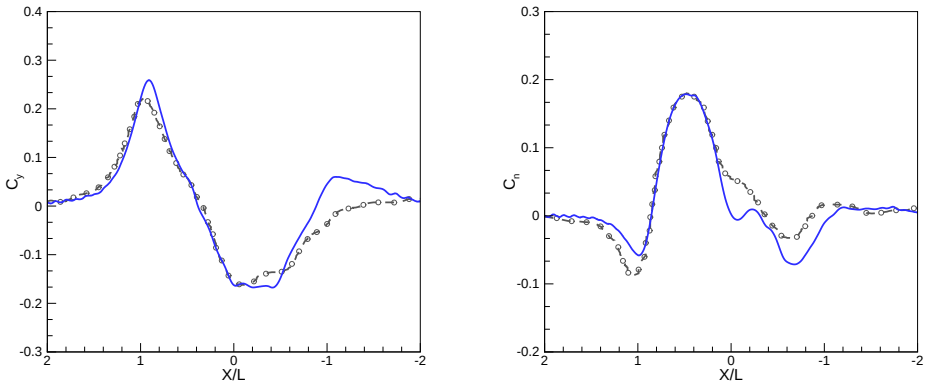

(b) $k = 0.141$

Figure 11: Relative velocity effects on the overtaken body. Side force (left) and yawing moment (right) coefficients. (⊖—) experimental, (—) numerical.

mental data. The comparison between the two previous numerical results, and a new case, $k = 0.331$ ($V_r = 15\ m.s^{-1}$), is illustrated in figure 12 with the addition of the drag force coefficient.

The evolution of the main coefficients when varying the relative velocity differs in the literature. Noger *et al* [6, 7] found that the aerodynamic coefficients are independent of the relative velocity. Corin *et al* [12] found that

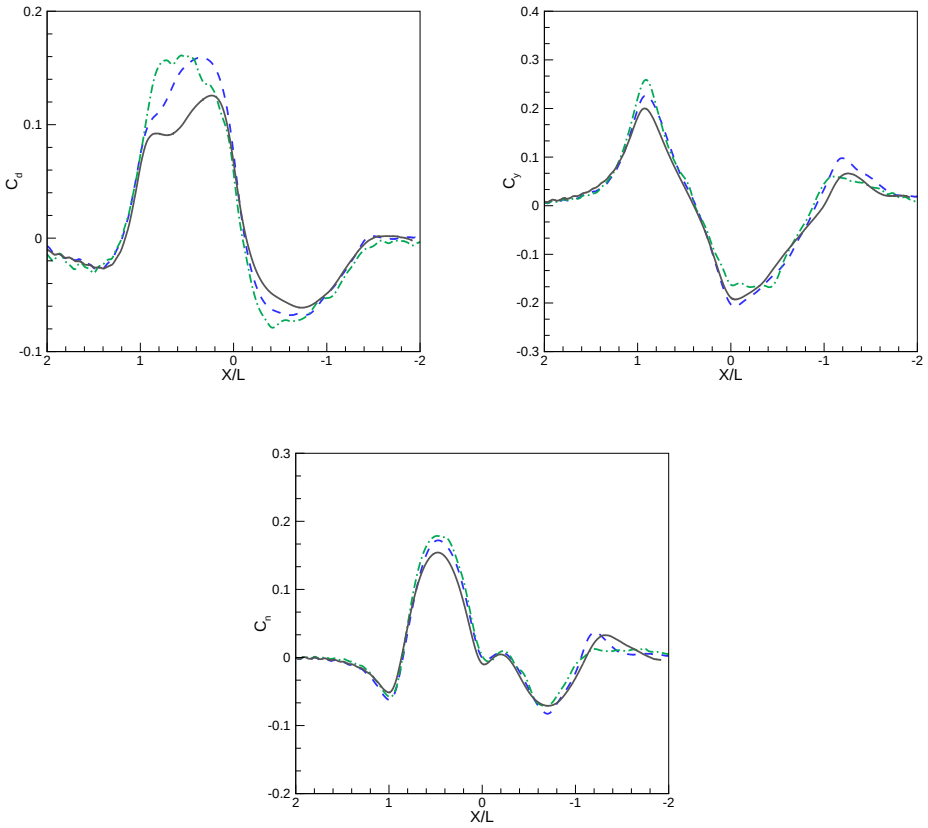

Figure 12: Relative velocity effects on the overtaken body. Drag force (top left), Side force (top right) and yawing moment (bottom) coefficients. (—) $k = 0.331$, (– –) $k = 0.248$, (– · –) $k = 0.141$.

when the relative velocity increased, the drag coefficient increased and the side force decreased. Clarke and Filippone [11], and Gilliéron and Noger [10], shown that an increase in relative velocity yields an increase in the peak coefficients. However, the coefficients are normalized with the velocity of the overtaken vehicle in [10, 11].

In the present study, the coefficients decrease when the relative velocity increases. When the relative velocity increases, the pressure field around the

overtaking vehicle becomes more substantial: its size is larger and the value of the dynamic pressure is more important. Therefore, the resulting forces occurring on the overtaken vehicle become more substantial. But these forces are normalized with the overtaking vehicle velocity which takes into account the relative velocity. This can explain the decrease of aerodynamic coefficients peaks.

5.5. Transverse spacing effects

In order to study the effects of the transverse spacing, the calculation $k = 0.248$ is carried out with two additional transverse spacing: $Y = 0.5W$ and $Y = 0.7W$. To perform these new calculations, a new mesh is made to take into account the substantial difference of transversal spacing between the case $Y = 0.25W$ and the case $Y = 0.5W$. This new mesh is deformed, in the transversal direction, for the calculation of the case $Y = 0.7W$.

The results, for the side force and the yawing moment coefficients, are shown in figure 13.

Both numerical results are in good agreement with the experimental data. Nevertheless, the numerical simulation underestimates the minimum value of the side force.

Figure 14 shows the evolution of the drag force coefficient, the side force coefficient and the yawing moment coefficient for the three different spacings. The last graph represents the evolution of the coefficient magnitudes as a function of the logarithm of the transverse spacing.

It can be easily seen that the coefficient amplitudes reduce when the transverse spacing increases. Besides, the effects occurring at X/L=0 and X/L=-1 are lower for the two highest spacings. The last graph shows that the evo-

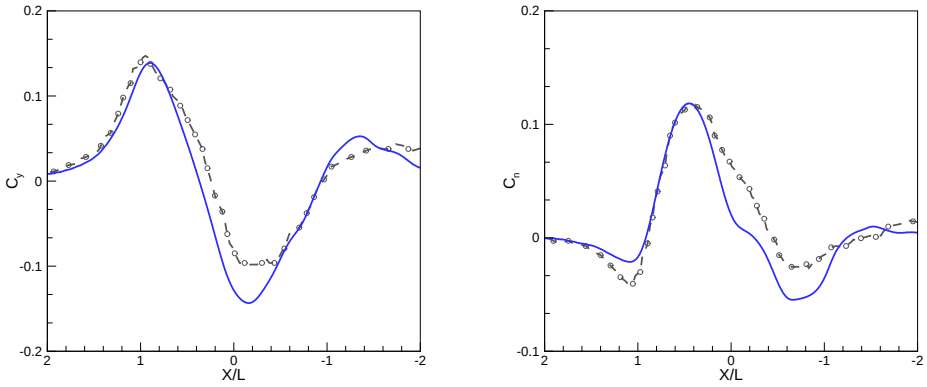

(a) $Y = 0.5W$

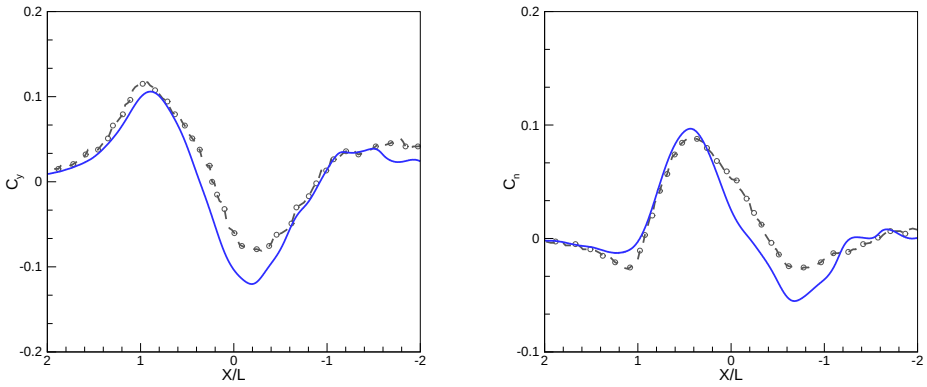

(b) $Y = 0.7W$

Figure 13: Transverse spacing effects on the overtaken body. Side force (left) and yawing moment (right) coefficients. (⊖—) experimental, (—) numerical.

lution of magnitudes is a linear function of the logarithm of the transverse spacing. This result was already shown by Noger *et al* [7].

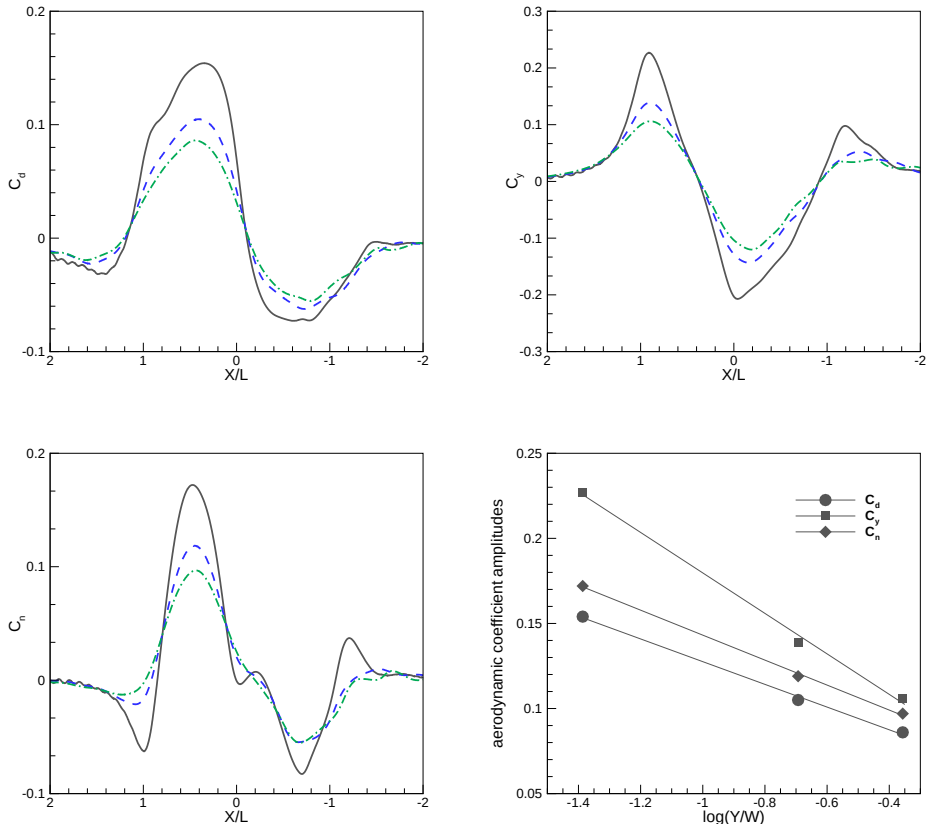

Figure 14: Transverse spacing effects on the overtaken body. Drag force coefficient (top left), side force coefficient (top right), yawing moment coefficient (bottom left) and coefficients magnitudes. (—) $Y = 0.25W$, (—) $Y = 0.5W$, (—) $Y = 0.7W$.

5.6. Overtaking vehicle

In order to study the effect on the overtaking vehicle, the moving vehicle is moved backwards, i.e. with a negative relative velocity. By doing this, the stationnary vehicle represents the overtaking vehicle and the measurements, in the experimental study, are possible. The comparison between experimental and numerical results are shown in figure 15 for a velocity ratio of $k = 0.196$.

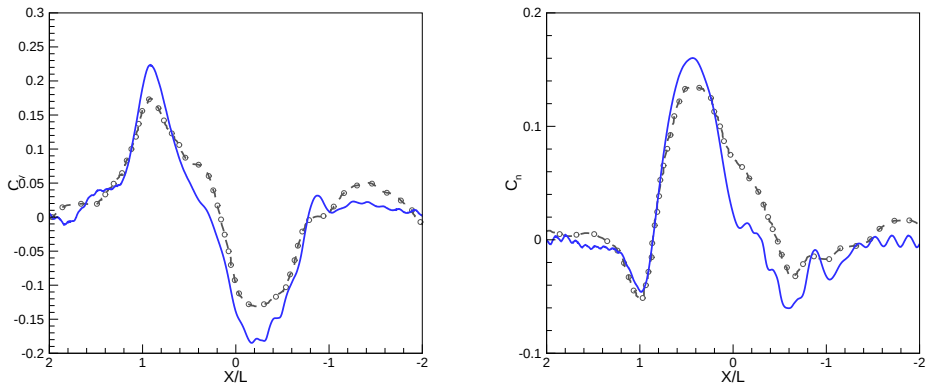

Figure 15: Effects on the overtaking body. Side force (left) and yawing moment (right) coefficients. (⊖) experimental, (—) numerical.

The behavior of the numerical curves are in agreement with the experimental results. However, the magnitudes of the side force and the yawing moment are more overestimated than for the overtaken vehicle.

5.7. Squareback bodies

The study of the 0° rear end body allows to highlight the capacity of the numerical methodology to reproduce the phenomena with a different geometry. For this case, the experimental drag force coefficient is available, and its results, experimental and numerical, are shown in figure 16 with the side force and the yawing moment coefficients. In order to highlight the effects induced by the squareback body, the numerical results obtained on the hatchback body are also shown. For a further comprehension, the experimental data of the squareback and the hatchback bodies are the same.

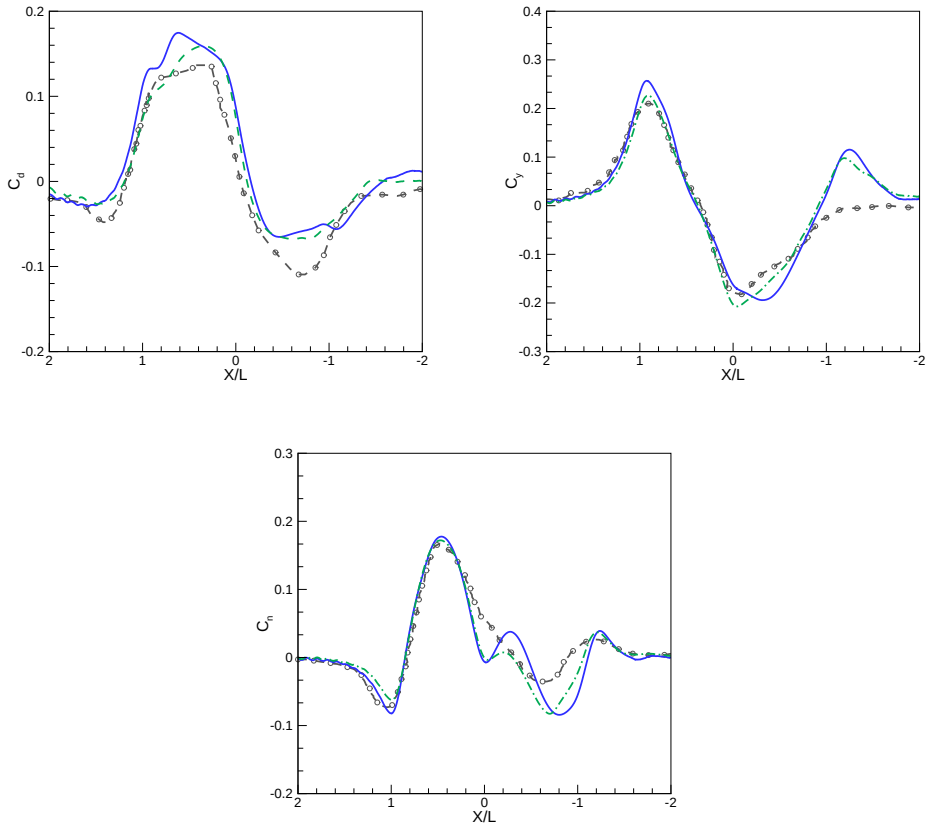

Figure 16: Effects on the squareback body. Drag force (top left), side force (top right) and yawing moment (bottom) coefficients. (⊖) experimental, (—) numerical results for the squareback body, (-·-) numerical results for the hatchback body.

5.7.1. Experimental/numerical comparison for the squareback bodies

The peaks of coefficients are slightly overestimated by the numerical results. However, numerical and experimental results are similar. The evolution of the drag force, for which this is the first comparison with experimental data, is well reproduced. Note that, in the numerical result, the prompt increase of drag force, at the position X/L=1, is subdivided in two. As for the increase of yawing moment at X/L=0, discussed previously, this result

appears on the experimental data for lower relative velocity, see [7].

5.7.2. Numerical comparison for the squareback and the hatchback bodies

It can be noted that for all the positions where flow separations effect have been remarked, i.e. X/L=1, X/L=0 and X/L=-1, the squareback body produces higher peaks. These flow separations come from the inner sharp edge at the aft of the bodies. The size of this sharp edge is 123.2 mm, see figure 1, for the slanted body while it is 201.6 mm for the squareback body. The separation flow effects are, then, more substantial.

6. Conclusions

A three-dimensional numerical methodology, with a deforming/sliding mesh method and the $\zeta - f$ turbulence modelling, was successfully employed to simulate the dynamic passing process between two vehicles. Studies have highlighted the capacities of the numerical method to well reproduce the effect of the relative velocity and of the lateral spacing on the aerodynamic forces and moments. A complete analysis has enabled to explain all the effects acting on the coefficients.

For the overtaken vehicle, it was shown that an increase of transversal spacing involves a decrease of aerodynamic coefficients amplitudes. Similarly, the aerodynamic coefficients peaks decrease when the relative velocity increases. The initial purpose of the project is to study some critical safety situations occurring during an overtaking. It was shown that the numerical set-up was suitable in the case of two identical vehicles overtaking, it remains to study two of the most substantial critical situations:

- when the overtaking occurs between vehicles with different sizes like a truck and a car
- when the vehicles are submitted to gusty winds and gusty crosswinds.

There is no reason to believe that the present numerical methodology fail to predict the good coefficients in a car-truck passing configuration.As for crosswinds, the effects are more difficult to reproduce with a RANS turbulence modelling.

Acknowledgments

This work is supported financially by the Area of Advance Transport at Chalmers. Software licenses were provided by AVL List GMBH. Computations were performed at SNIC (Swedish National Infrastructure for Computing) at the Center for Scientific Computing at Chalmers (C3SE) and National Supercomputer Center (NSC) at Linköping University.

References

[1] R. K. Heffrey, Aerodynamics of passenger vehicles in close proximity to trucks and buses, SAE paper (1973) 901 – 914.

[2] J. P. Howell, The influence of the proximity of large vehicle on the aerodynamic characteristics of a typical car. advances in road vehicle aerodynamics, bhra, fluid engineering (1973) 207 – 221.

[3] T. Legouis, P. Bourassa, V. D. Nguyen, Influence d'un poids lourd équipé ou non de dispositifs aérodynamiques sur une automobile en manœuvre

de dépassement, Journal of Wind Engineering and Industrial Aerodynamics 9 (1984) 381 – 387.

[4] D. P. Telionis, C. J. Fahrner, G. S. Jones, An experimental study of highway aerodynamic imterferences, Journal of Wind Engineering and Industrial Aerodynamics 17 (1984) 267 – 293.

[5] S. Yamamoto, K. Yanagimoto, H. Fukuda, H. China, K. Nakagawa, Aerodynamic influence of a passing vehicle on the stability of the other vehicles, JSAE Review 18 (1997) 39 – 44.

[6] C. Noger, E. Széchényi, Experimental study of the transient aerodynamic phenomena generated by vehicle overtaking, 8th International Conference on Flow-Induced Vibrations (FIV), Ecole Polytechnique, Paris (France) (2004).

[7] C. Noger, C. Regardin, E. Széchényi, Investigation of the transient aerodynamic phenomena associated with passing manoeuvres, Journal of Fluids and Structures 21 (2005) 231 – 241.

[8] S. R. Ahmed, G. Ramm, G. Faltin, Some salient features of the time averaged ground vehicle wake (1984). SAE Paper 840300.

[9] C. Noger, E. V. Grevenynghe, On the transient aerodynamic forces induced on heavy and light vehicles in overtaking processes, Int. J. Aerodynamics 1 (2011) 373 – 383.

[10] P. Gilliéron, C. Noger, Contribution of the analysis of transient aerodynamic effects acting on vehicles, SAE paper no. 2001-01-1311 (2004).

[11] J. Clarke, A. Filippone, Unsteady computational analysis of vehicle passing, Journal of Fluid Engineering 129 (2007) 359 – 367.

[12] R. J. Corin, L. He, R. G. Dominy, A CFD investigation into the transient aerodynamic forces on overtaking road vehicle models, Journal of Wind Engineering and Industrial Aerodynamics 96 (2008) 1390 – 1411.

[13] P. Gilliéron, Detailed analysis of the overtaking process, Journal of Mechanical Engineering 53 (2003).

[14] K. Hanjalić, M. Popovac, M. Hadžiabdić, A robust near-wall elliptic-relaxation eddy-viscosity turbulence model for CFD, International Journal of Heat and Fluid Flow 25 (2004) 1047–1051.

[15] P. A. Durbin, Near-wall turbulence modeling without damping functions, Theretical and Computational Fluid Dynamics 3 (1991) 1–13.

[16] C. G. Speziale, S. Sarkar, T. B. Gatski, Modelling the pressure-strain correlation of turbulence: an invariant dynamical systems approach, Journal of Fluid Mechanics 227 (1991) 245–272.

[17] S. Krajnović, E. Bjerklund, B. Basara, Simulations of the flow around high-speed train meeting each other at the exit of a tunnel, 21st International Symposium of Dynamics of Vehicles on roads and Tracks (2009).